JGR Planets

RESEARCH ARTICLE
10.1029/2018JE005733

**Key Points:**
- The thermal inertia of the surface of Ceres has been derived using spatially resolved data from the Dawn mission
- The Haulani crater appears to have a higher thermal inertia with respect to Ceres's average
- The average thermal inertia of the surface of Ceres appears to have low values (1–15 $J \cdot m^{-2} \cdot s^{-½} \cdot K^{-1}$)

**Correspondence to:**
E. Rognini,
edoardo.rognini@iaps.inaf.it

**Citation:**
Rognini, E., Capria, M. T., Tosi, F., De Sanctis, M. C., Ciarniello, M., Longobardo, A., et al (2020). High thermal inertia zones on Ceres from Dawn data. *Journal of Geophysical Research: Planets*, *125*, e2018JE005733. https://doi.org/10.1029/2018JE005733

Received 26 JUN 2018
Accepted 18 JUL 2019
Accepted article online 30 JUL 2019

**Author Contributions:**
**Conceptualization:** E. Rognini
**Data curation:** F. Tosi, A. Frigeri, S. Fonte, M. Giardino, E. Ammannito
**Formal analysis:** E. Rognini
**Investigation:** A. Longobardo, F. G. Carrozzo, C. T. Russell
**Methodology:** E. Rognini, M. T. Capria, M. Ciarniello, S. Fonte
**Project administration:** M. C. De Sanctis, C. A. Raymond, C. T. Russell
**Resources:** F. Tosi, A. Frigeri, S. Fonte, M. Giardino, E. Ammannito
**Software:** M. Giardino
**Supervision:** M. T. Capria, M. C. De Sanctis
**Validation:** M. T. Capria
**Writing - original draft:** E. Rognini
**Writing – review & editing:** M. T. Capria, F. Tosi, M. C. De Sanctis, M. Ciarniello, A. Longobardo, F. G. Carrozzo, A. Raponi, E. Palomba, S. Fonte, C. T. Russell



# High Thermal Inertia Zones on Ceres From Dawn Data

**E. Rognini[1], M. T. Capria[1], F. Tosi[1], M. C. De Sanctis[1], M. Ciarniello[1], A. Longobardo[1], F. G. Carrozzo[1], A. Raponi[1], A. Frigeri[1], E. Palomba[1], S. Fonte[1], M. Giardino[2], E. Ammannito[2], C. A. Raymond[3], and C. T. Russell[4]**

[1]INAF-IAPS, Rome, Italy, [2]ASI-SSDC, Rome, Italy, [3]California Institute of Technology, JPL, Pasadena, CA, USA, [4]Department of Earth, Planetary, and Space Sciences, University of California, Los Angeles, CA, USA

**Abstract** Thermal inertia is a key information to quantify the physical status of a planetary surface. We derive the thermal inertia of the surface of Ceres using spatially resolved data from the Dawn mission. For each location, this quantity can be constrained by comparing theoretical and observed diurnal temperature profiles from retrieved temperatures. We calculated Ceres's surface theoretical temperatures with a thermophysical model that provides temperature as a function of thermal conductivity and roughness, and we determined the values of those parameters for which the best fit with the observed data is obtained. Our results suggest that the area of crater Haulani displays thermal inertia values (up to 130–140 $J \cdot m^{-2} \cdot s^{-½} \cdot K^{-1}$) substantially higher than the very low to low values (from 1–15 to 50–60 $J \cdot m^{-2} \cdot s^{-½} \cdot K^{-1}$) derived for the overall surface of Ceres. The results are more ambiguous for the bright faculae located in the floor of crater Occator.

**Plain Language Summary** We have calculated Ceres's surface temperatures and we have compared them with the observations. We have used new high-resolution data provided by the Dawn/National Aeronautics and Space Administration mission, which was launched in 2007 with the aim of studying two of the largest bodies of the Main Belt: Vesta and Ceres. Our results suggest that the surface is made of fine-grained material, according to previous analysis made by other authors by using other independent data and methods. We have also studied two particular areas of Ceres that shows peculiar properties (albedo and/or chemical/physical structure).

## 1. Introduction and Background

Ceres is the largest body (average diameter of 945 km) in the Main Asteroid Belt and was the first and former largest asteroid to be discovered by Giuseppe Piazzi, on 1 January 1801. The planet-like nature of Ceres and its survival from the early stages of the Solar System make it an important object for understanding the planetary evolution.

Gravity measurements indicate that Ceres is nearly at hydrostatic equilibrium and has a denser core and low-density mantle and crust (Park et al., 2016). Ceres's mass, deduced from the orbital parameters of the spacecraft Dawn, is $9.384 \pm 0.001 \times 10^{20}$ kg, and the dimensions are 483.1 by 481.0 by 445.9 km (Russell et al., 2016). Ceres appears to be differentiated into a rocky core and an icy mantle and may have a remnant internal ocean of liquid water under the layer of ice (McCord & Sotin, 2005; Park et al., 2016); its bulk density of about 2 $g/cm^3$ suggests a water content between 17% and 27% by mass. Ceres belongs to the C-complex asteroids (75% of the known asteroids; De Meo et al., 2015); that is, its composition includes a large amount of carbon and is characterized by a low albedo. The analysis of data returned by Dawn suggests that the surface of Ceres has been probably covered by an ocean of water and ammonia; when this ocean froze and sublimated, salt deposits formed across the surface (Carrozzo et al., 2018). The surface of Ceres is dark, with an average modeled geometric albedo of $0.094 \pm 0.007$ (Ciarniello et al., 2017), and is dominated by a dark, spectrally featureless and yet unidentified component, mixed with magnesium phyllosilicates, ammoniated phyllosilicates, and magnesium carbonates at global/broadly regional scale (Ammannito et al., 2016; De Sanctis et al., 2016; Carrozzo et al., 2018), with calcium and sodium carbonates showing up at specific locations (Carrozzo et al., 2018). Ceres appears to be icy (De Sanctis et al., 2016; De Sanctis et al., 2018); Dawn detected water ice in about 10 specific locations (e.g., Combes et al., 2016; Platz et al., 2016) but did not find endogenic sources (e.g., vapor plumes) that could explain the transient behavior of the atmosphere.

The Dawn/National Aeronautics and Space Administration mission was launched in 2007 with the goal of investigating two of the largest bodies in the Main Belt: Vesta and Ceres. The spacecraft hosted three instruments: the framing camera (FC; Sierks et al., 2011), the visual and infrared mapping spectrometer (VIR; De Sanctis et al., 2011), and the Gamma Ray and Neutron Detector (Prettyman et al., 2011). VIR operates in the spectral range from the near ultraviolet to the near infrared (0.25–5.1 μm); it achieved global, regional and local hyperspectral coverage of both Vesta and Ceres. VIR data are stored as hyperspectral images or "cubes," including hundreds of bi-dimensional images, each acquired at a specific wavelength in the above range. Dawn orbited around Ceres from March 2015 to November 2018. The orbital mission at Ceres was organized in different phases, characterized by different altitudes over the surface implying variable VIR pixel ground resolution. The main phases were Rotational Characterization orbit, SURVEY, High Altitude Mapping Orbit (HAMO), and Low-Altitude Mapping Orbit. Each phase was further divided into cycles (see Table 1 and Figure 1).

While the primary scientific objective of VIR was to determine and map the surface mineralogy, the long-wavelength component of the spectra ($4.5\ \mu m < \lambda < 5.1\ \mu m$) can be used to retrieve the surface temperature through a Bayesian approach (Tosi et al., 2014); the retrieval is applied separately on each pixel unaffected by detector saturation. The VIR instrument can sense temperatures within the uppermost surface layer as thick as tens of microns; in the sampled spectral range the temperature is a non-linear function of radiance, with a larger weight of the hottest subpixel features, so the obtained value is representative of the subpixel regions at higher temperatures modulated by their effective areas. Temperature values retrieved in this way show an accuracy better than 3 K above 180 K, and better than 1 K above 210 K, while values below 180 K have increasingly worse accuracy. The lower limit of temperatures sensed by the instrument is dictated by the in-flight instrumental noise, varying over time depending on a number of parameters, most notably the spectrometer's temperature.

Knowledge of the retrieved surface temperature and of the true local solar time at which the data were acquired allows one to derive a daily temperature curve, surface temperature as function of local solar time, which is key in estimating the thermal inertia (Audouard et al., 2014; Delbo et al., 2015; Neugebauer et al., 1971). Thermal inertia is a fundamental parameter that controls the surface temperature variations of atmosphereless bodies and measures the velocity of penetration of the thermal wave controlling the surface temperature. It is defined as

$$T.I. = \sqrt{k\rho c}\ \left(\mathrm{Jm^{-2}s^{-\S}K^{-1}}\right) \tag{1}$$

where $k$ is the thermal conductivity, $\rho$ the density, and $c$ is the specific heat. The daily temperature curve of a specific area is strongly dependent on the physical and thermal properties of the first centimeters of soil, so determining the thermal inertia of the surface of an atmosphereless body provides an insight into the structure and physical properties of that surface, giving indications on the type (e.g., dust, regolith, or rock) and the evolution of the surface material (Harris & Lagerros, 2002). Capria et al. (2014) built a global map of thermal inertia for Vesta by using disk-resolved temperature data retrieved by VIR at coarse spatial resolution (1.3 km per pixel), which covered a relatively broad range of local solar times from the local morning to the local evening. Instead, in this work we focused only on VIR data acquired in the Survey (1.1 km per pixel) and HAMO (0.38 km per pixel) mission stages, which due to operational constraints span a narrower range of local solar times, concentrated mostly in the local morning. It should also be noted that VIR is not sensitive to nighttime temperatures, which are way below its lower limit of sensitivity (~180 K). However, taking into account the characteristics of the soil of the Ceres's surface and other thermal inertia estimates provided in the literature, we can determine a range of plausible thermal inertia and subpixel roughness values. In this work we have analyzed two areas of the surface showing unique characteristics, with the aim of finding any thermal inertia deviations from Ceres's average: Haulani crater and the bright faculae in Occator crater.

The 34-km-diameter crater Haulani, one of the youngest craters on the surface of Ceres (<6 Ma), is located in the equatorial region at 5.8°N,10.77°E and is the fourth largest crater within the quadrangle Ac-H-6 "Haulani" (Roatsch et al., 2016). The Haulani area is peculiar because the crater's ejecta show a spectrally distinct signature, with very reduced or even negative spectral slope from the visible to the near infrared up to 2.25 μm (Tosi et al., 2018, 2019). Albedo maps retrieved in the near infrared indicate a mixture of dark and bright materials (Tosi et al., 2018, 2019). Furthermore, the spectral features at 2.7 and 3.1 μm indicate a

**Table 1**
*Characteristics of the Mission Phases of Dawn Around Ceres*

| Mission phase | Starting date | End date | Altitude (km) | Pixel ground resolution (m) |
|---|---|---|---|---|
| RC3 | 23 April 2015 | 9 May 2015 | 13,522–13,637 | 3,380–3,409 |
| SURVEY | 6 June 2015 | 30 June 2015 | 4,380–4,423 | 1,095–1,106 |
| HAMO | 17 August 2015 | 23 October 2015 | 1,450–1,475 | 363–369 |
| LAMO | 16 December 2015 | 2 September 2016 | 355–403 | 89–101 |

*Note*. In the last column the pixel ground resolution of the imaging spectrometer visual and infrared mapping spectrometer is shown. RC3 = Rotational Characterization orbit; HAMO = High Altitude Mapping Orbit; LAMO = Low-Altitude Mapping Orbit.

decrease of Mg-bearing phyllosilicates and ammoniated phyllosilicates in the floor of the crater and the bright ejecta; the degree of mixing of these phases increases from the northwest to the southeast of the crater. The area also shows a local enhancement of calcium and possibly sodium carbonate minerals: this is an indication of hydrothermal processes that followed the impact (Tosi et al., 2018, 2019). Crater Haulani shows the most distinct thermal contrast across the entire surface of Ceres: This thermal contrast was first detected during the Approach phase in February 2015: at the coarse spatial resolution of those early VIR data (11.4 km per pixel), a temperature difference of 5 K in Haluani compared to surrounding areas was highlighted, which at that spatial scale could not be due to shading effects induced by topography (Tosi et al., 2019). On the basis of HAMO data acquired later at a VIR pixel resolution of 0.38 km per pixel, the central mountainous ridge of Haulani was found to be ~15 K cooler than the crater's western floor as observed, within the same VIR images, at the same local solar time and under similar instantaneous solar illumination conditions (Tosi et al., 2018).

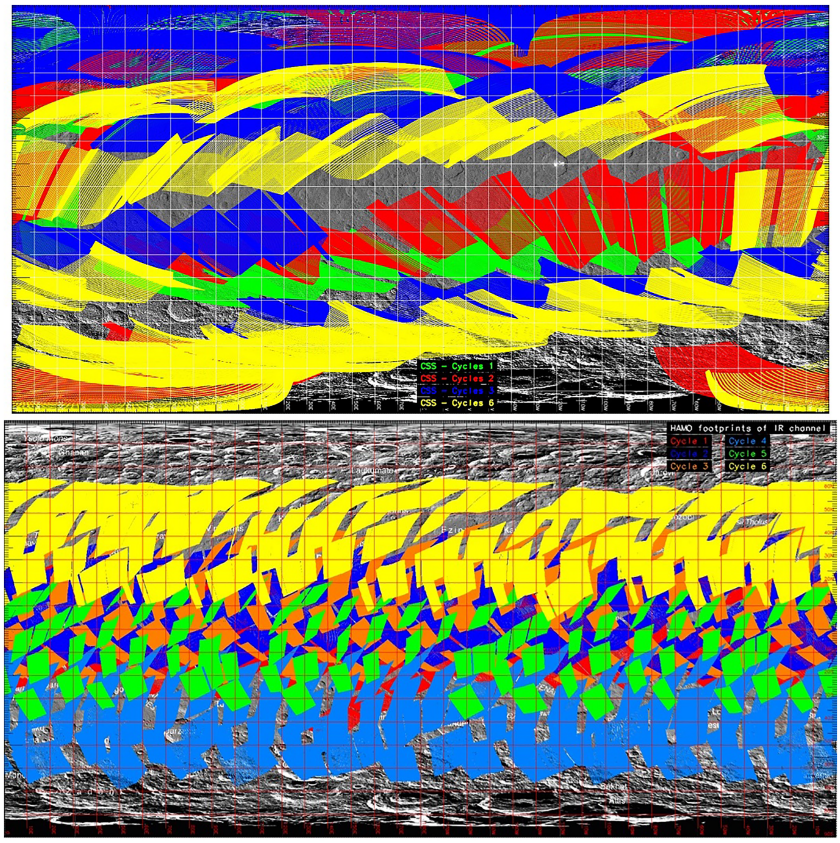


**Figure 1.** Data coverage of the mission phases considered in this work: Survey (top figure) and High Altitude Mapping Orbit (bottom figure). The different colors refer to the different cycles of the corresponding phases (see text).

The second area that we have analyzed in detail is Occator, a 92-km-diameter crater located at 19.86°N 238.85°E and showing a cluster of bright spots. This cluster is formed by a very bright spot in the center of the crater (*Cerealia Facula*), and a second group of spots in the eastern floor (*Vinalia Facula*). From the spectral slopes it can be inferred that the crater interior is younger than the crater walls, and the white material of the faculae is likely much younger. Crater counting estimations gave 34 ± 2 Ma for Occator (Nathues et al., 2015) and 6.9 ± 0.9 Ma for the floor material (Nathues et al., 2016). The crater shows mass deposits that originate from the wall and extend to the floor for 10–20 km; at SW and NE these deposits are covered by floor material that extends from the center. The features of these morphological structures, the presence of fractures and their orientation and age, the central depression all suggest postimpact processes as hydrothermal processes and evaporation and emplacement of flow materials (Jaumann et al., 2017). The bright spots are areas characterized by high albedo values (up to 40%), and their spectra suggest that they are composed by a mixture of anhydrous sodium carbonate or natrite ($Na_2CO_3$) and ammonium chloride ($NH_4Cl$) or ammonium bicarbonate ($NH_4HCO_3$; Carrozzo et al., 2018; Palomba et al., 2019); their origin is probably due to a relatively recent crystallization of brines that reached the surface from the interior (Stein et al., 2017).

## 2. Thermophysical Analysis of the Surface of Ceres

### 2.1. The Thermophysical Model

In order to determine the thermal inertia from measured temperatures, a thermophysical model is required (e.g., Rozitis & Green, 2011). The one-dimensional model we used (Capria et al., 2014) solves the heat conduction equation and provides theoretical temperatures as a function of conductivity, albedo, emissivity, density, and specific heat; the model is applied to a detailed shape model of Ceres in order to take into account the instantaneous illumination (Raymond et al., 2011; Preusker et al., 2016). A finite-differences scheme is used to solve the 1-D heat transport equation, applied to each of the layers into which the internal radius has been subdivided:

$$\rho c \frac{\partial T}{\partial t} = \frac{\partial}{\partial x}\left(k \frac{\partial T}{\partial x}\right) \tag{2}$$

where $\rho$ is the density, $c$ the specific heat, $T$ the temperature, $t$ the time, $x$ the depth, and $k$ is the thermal conductivity. The thickness of the layers is 0.05 cm close to the surface and is increasing toward the interior of the body (logarithmic grid). The surface boundary condition is written as follows:

$$\frac{S(1-A)\mu}{r^2} = X\sigma T^4 + k\frac{\partial T}{\partial x} \tag{3}$$

where $S$ is the solar constant, $A$ is the Bond albedo, $\mu$ is the illumination angle cosine, $r$ is the heliocentric distance in astronomical unit, $k$ is the thermal conductivity, $\sigma$ is the Stefan-Boltzmann constant, and $X = (1 - \varepsilon\xi)\varepsilon$ is a "roughness parameter" where $\varepsilon$ is the emissivity and $\xi$ is the subpixel roughness. $\xi$ (Lagerros, 1998) has been introduced to characterize the topography (roughness) on subpixel scale, that means it can be regarded as a measure of the surface irregularity at a scale smaller than the shape model (~140 m in this specific case) and larger than the thermal skin depth (of the order of 1 cm, expressed, in the case of the diurnal cycle, as $D = \sqrt{\frac{kP}{\pi\rho C}}$ where $P$ is the rotation period); it can be interpreted, for example, as the percentage of cratered terrain with respect to flat terrain (Keihm et al., 2012; Müller & Lagerros, 1998). Roughness (Davidsson et al., 2015) is thought to be the cause of thermal-infrared beaming, the phenomenon for which a surface emits in a non-Lambertian way with a tendency to reradiate the absorbed radiation toward the Sun. The beaming is originated by the multiple scattering between the surface elements, increasing the amount of energy absorbed by the surface, and by the fact that surface elements oriented toward the Sun will become much hotter than a flat surface. Flat surfaces will have $\xi$ values close to 0, while very irregular surfaces will have values approaching unity; high values of $\xi$ will increase the computed surface temperature, while low values will have an opposite effect.

The thermophysical model is applied to a given location (specified by latitude, longitude and the corresponding illumination condition). Ceres is followed along its orbit during the simulation; in order to stabilize the results of the computation, the code is run on more than one orbit, until the temperatures of two consecutive

orbits differ by less than 0.01 K. Lateral heat conduction can be neglected because the facets of the shape model on which the thermophysical model is applied are always larger than the thermal skin depth. The illumination condition, for each time step and location on the shape model, is obtained through SPICE-based software and navigational databases, the so-called "SPICE kernels" (Acton, 1996).

The albedo of a given location is calculated by conversion of a reflectance map at 1.2 μm (Ciarniello et al., 2017); the average spectrum of Ceres is nearly flat, and the reflectance at 1.2 μm is a good proxy for the reflectance at 0.55 μm (the peak of the solar spectrum), with differences of a few percent (e.g., Rivkin et al., 2011).

We are assuming that the surface is covered by a meters thick layer of particulate material whose density is minimum on the surface and increases with the depth (see Table 2) following an empirical exponential law (Cremers & Hsia, 1973):

$$\rho(z) = \rho_{\max} \frac{z + 12.2}{z + 18} \tag{4}$$

where $z$ is the depth expressed in centimeters.

The thermal conductivity has the form

$$k(T) = k_c + k_r T^3 \tag{5}$$

where $k_c$ and $k_r$ are the conductive and radiative terms; the first term takes into account the conductive transfer across the particles, and the second term takes into account the radiative heat transfer, sensible at high temperatures. Different kinds of particulate material, ranging from very fine dust to incoherent rocky debris (regolith), can be simulated in the code. To each type of material, a density profile, with values increasing with depth, has been associated. Thermal conductivity is taken into account through empirical expressions ($k_c$ and $k_r$) depending on density and temperature and based on the properties of the chosen particulate material, which have been derived from ground and spacecraft observations, lunar in situ measurements and lunar returned samples (Capria et al., 2014; Cremers & Hsia, 1973; Vasavada et al., 2012; Vasavada & Paige, 1999). The empirical expressions for the terms in equation (5) are

$$k_{c,r} = \begin{cases} k_{c,r}^{(0)} & z<1 \\ k_{c,r}^{(0)} + a\left(\frac{\rho(z)-\rho(1)}{\rho_{max}-\rho(0)}\right)^b & z>1 \end{cases} \tag{6}$$

where $z$ is expressed in centimeters, the subscripts "$c$" and "$r$" refer to the conductive and radiative term, $k_c^{(0)} = 10^{-3}, k_r^{(0)} = 2.8{\times}10^{-11}$, $b = 0.35, a = \{0.0092, 3.4{\times}10^{-10}\}_{c,r}$, and the densities refer to the specific simulated material (Table 2).

Experiments suggest that the thermal conductivity largely depends on the physical structure of the soil and not on composition (Opeil et al., 2012), so we can use the expressions used in Capria et al. (2014), also for the surface of Ceres whose composition is very different from the basaltic one typical of Vesta. Typical thermal conductivity values range from about $10^{-3}$ (fine dust) to 0.02 $W{\cdot}m^{-1}{\cdot}K^{-1}$ (regolith) at the temperature range of the simulations (from 60 to 240 K).

Specific heat is temperature dependent and is derived from a fit of experimental measurements of materials compatible with Ceres surface (Biele et al., 2014):

**Table 2**
*Density Ranges for the Materials Considered in This Work*

| Material | Maximum density ($kg/m^3$) | Thermal inertia ($J{\cdot}m^{-2}{\cdot}s^{-1/2}{\cdot}K^{-1}$) |
|---|---|---|
| Fine dust | 1,800 | 1–16 |
| Fine regolith | 1,950 | 50–65 |
| Regolith | 1,950 | 110–140 |

*Note*. The hypothesis is made that density is increasing with depth: The minimum density is found on the surface.

**Table 3**
*Characteristics of the Area and the Points Selected for the Analysis in the Haulani Crater. The roughness of the floor point has not been identified.*

| Area | Longitude range (°) | Latitude range (°) | Local time range (hr) | Thermal inertia value ($J{\cdot}m^{-2}{\cdot}s^{-1/2}{\cdot}K^{-1}$) | $\xi$ |
|---|---|---|---|---|---|
| Haulani crater | [9.8, 12] | [4.5, 6.8] | [9.5, 11.5] | 115–136 | 0.55 |
| Peak | 10.58 | 6.04 | [9.18, 11.24] | 110–130 | 0.38 |
| Floor | 10.37 | 5.21 | [9.23, 11.1] | ≥130 | ? |

$$c(T) = a + b(T-T_0) + c(T-T_0)^2 + d(T-T_0)^3 \quad (7)$$

where $T_0 = 250\ K, a = 633, b = 2.513, c = -0.0022$, and $d = -2.8 \times 10^{-6}$.

### 2.2. Thermal Inertia Determination

We performed the analysis of the thermal properties of the surface of Ceres by using the same procedure previously adopted for Vesta (Capria et al., 2014). We selected the data from the Survey and HAMO mission phases, as they display a good tradeoff between coverage and pixel resolution compared to other mission phases (Figure 1). In particular, HAMO data have a pixel resolution ~2.9 times higher than Survey data (~0.38 versus ~1.1 km per pixel).

In order to retrieve the average thermal inertia of Ceres, we divided the surface into rectangular areas with angular bins of 2° in both longitude and latitude. Conversely, the Haulani and Occator craters were analyzed locally, that is, by considering only the area covered by of those craters (Tables 3 and 4). A retrieved temperature ($T_r$) represents the average temperature, at the time and date of the observation, measured on an area defined by the instantaneous field of view of a VIR pixel; to each pixel a planetocentric latitude and longitude are associated, derived from the geometry information associated to VIR data. All the $T_r$ values, or measured data points, can be assigned to a given area, on the basis of their latitude and longitude; when analyzing the average thermal inertia, we have identified the areas displaying the highest number of measured data points and selected those areas for our analysis (Table 5). In our process of data selection, we have further discarded the data points with uncertainties associated to retrieved temperature values greater than 5 K and those with a phase angle greater than 30°. The reason for the latter choice is that our thermophysical code calculates the temperature we would measure if we were at the local zenith of the surface, while $T_r$ values are affected by the illumination geometry; by considering observed temperature with small phase angles we are minimizing the effect of the illumination geometry.

For every area analyzed in this work we have a set of time-temperature data:

$$\{t_i, T_{\mathrm{theo},i}\}, i = 1, ..., N$$

where $t_i$ is the local solar time, $T_{r,i}$ is the corresponding retrieved temperature, and $N$ is the number of data points (typically greater than 200). For every area we then select a set of $M$ points (with $M < N$, typically $M =$ 4 or 5) that can be considered as representatives of the area. As an example, in Figure 2a we show the area with longitude-latitude ranges [92°E, 94°E] × [6°S, 4°S]; the parallel dotted lines correspond to four VIR cubes acquired in this area, at different times, and the red dots are the selected locations. We fix a thermal conductivity class and, for every selected point (with progressive number $c = 1,...,M$), we calculate a set of theoretical temperature curves $T^c_{\mathrm{theo}}(t, \xi)$ as a function of roughness $\xi$ (Figure 2b). Then we define a chi-square function as follows:

**Table 4**
*Characteristics of the Areas Selected for the Analysis of the Bright Spots of the Occator Crater*

| Area | Longitude range (°) | Latitude range (°) | Local time range (hr) | Thermal inertia values ($J{\cdot}m^{-2}{\cdot}s^{-1/2}{\cdot}K^{-1}$) | $\xi$ |
|---|---|---|---|---|---|
| Cerealia facula | [239.5, 239.8] | [19.5, 19.85] | 9.5–11.5 | 10 ± 2 or 135 ± 5 | 0.5–0.9 |
| Vinalia facula | [242.44, 242.96] | [20.17, 20.42] | 10.3–11.2 | 9 ± 8 or 135 ± 5 | 0.2–0.65 |

**Table 5**
*Characteristics of the Rectangular Areas Selected for the Analysis, With the Local Time Range of Observed Data and Results for the Average Thermal Inertia*

| Area | Longitude range (°) | Latitude range (°) | Local time range (hr) | Thermal inertia value ($J \cdot m^{-2} \cdot s^{-1/2} \cdot K^{-1}$) | $\xi$ |
|---|---|---|---|---|---|
| 1 | [92,94] | [−6,−4] | 9.5–11.5 | 1–15 | $0.15 \pm 0.05$ |
| 2 | [132,134] | [16,18] | 8.7–11.5 | 1–15 | $0.2 \pm 0.05$ |
| 3 | [146,148] | [34,36] | 9.5–12.5 | 1–15 | $0.2 \pm 0.05$ |
| 4 | [178,180] | [−26,−24] | 10–13 | 1–15 | $0.2 \pm 0.05$ |
| 5 | [262,264] | [0,2] | 9–12 | 1–15 | $0.2 \pm 0.05$ |
| 6 | [300,302] | [0,2] | 9.5–13 | 1–15 | $0.2 \pm 0.05$ |
| 7 | [18,20] | [44,46] | 11.5–14 | 1–15 | $0.2 \pm 0.05$ |
| 8 | [278,280] | [−14−12] | 11.5–13 | 1–15 | $0.2 \pm 0.05$ |
| 9 | [170,172] | [−28,−26] | 11.5–13 | 1–15 | $0.2 \pm 0.05$ |
| 10 | [12,14] | [42,44] | 11.5–13.5 | 1–15 | $0.2 \pm 0.05$ |

$$\chi^2(\xi) = \frac{\sum_{c=1}^{M} \sum_{i=1}^{N} \left( \frac{T_{r,i} - T^{C}_{\mathrm{theo},i}(\xi)}{\sigma_i} \right)^2}{\delta T^2 M \sum_{i=1}^{N} \frac{1}{\sigma_i^2}} \tag{8}$$

where $T^{C}_{\mathrm{theo,i}}(\xi)$ is the $c$th calculated temperature at the local solar time $t_i$ with roughness $\xi$ and $\delta T$ is the typical temperature dispersion in the observed data (5–10 K for the areas with a high number of points, few kelvins in other cases). This function has to be minimized with respect to $\xi$, and the process is repeated for every material class. Once a satisfactory temperature curve has been calculated, a thermal inertia value is derived from thermal conductivity, density, and specific heat capacity (equation (1)). We recall that, especially at low thermal conductivity, thermal inertia is temperature dependent; the thermal inertia ranges we found correspond to the temperature ranges of the simulations, covering the full diurnal cycles on Ceres (e.g., the temperature for low thermal inertia case in most of the areas typically goes from 60–70 to 240–250 K).

This procedure has been performed for all of the selected rectangular areas and the crater areas and is based on the fundamental hypothesis that if, for a given set of input parameters, the theoretical temperatures are matching the measured ones within the associated uncertainties, then the values assigned to the parameters set should correspond to the real values describing the local terrain properties.

This procedure has been adopted because temperature retrieved data were already available; moreover, in this way, it is easier to simulate the effect of different kind of materials using empirical expressions derived

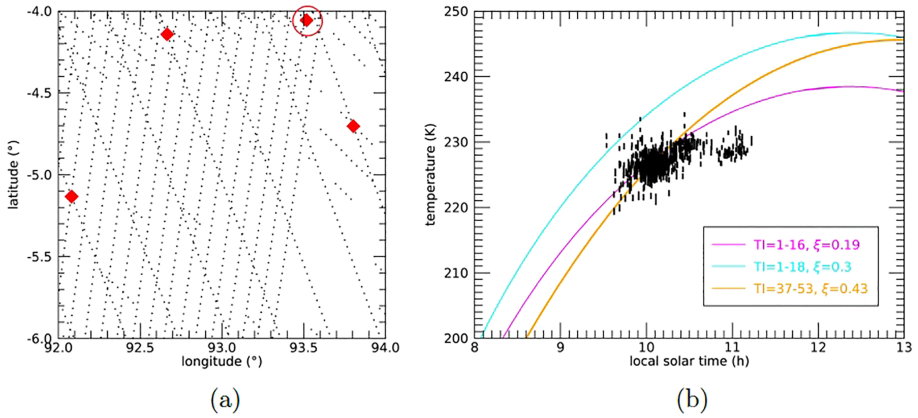


**Figure 2.** (a) Available observation points in the first area (see the text and Table 5) from the High Altitude Mapping Orbit data set. The dots represent all the visual and infrared mapping spectrometer-derived surface temperature points with associated uncertainties <5 K and phase angle <30°, whereas the red diamonds represent the locations that have been selected for the calculation of the theoretical temperature profiles. The circled red diamond has been used for the calculation of the theoretical curves shown in the plot on the right. (b) Comparison between observed temperatures (black bars) and theoretical temperature curves corresponding to different materials and roughness values.

from extraterrestrial samples. A disadvantage is that we are necessarily limited, in the analysis, to the data with low phase angles.

## 3. The Results

### 3.1. Higher Thermal Inertia Areas: The Haulani and Occator Craters

A specific analysis was then performed on the two locations of Ceres with possible peculiar thermal inertia values, that is, the Haulani crater and the bright faculae in crater Occator. The latter is the cluster of the brightest spots on Ceres (De Sanctis et al., 2016; Longobardo et al., 2017, 2019), whereas Haulani is another bright and blue area (Tosi et al., 2019).

#### 3.1.1. The Haulani Crater

The results of the thermal analysis of crater Haulani are shown in Figure 3. Fine dust and regolith (Table 2) have been considered to simulate the surface material in this area. The retrieved temperature data have a large scattering, so they can be fitted by theoretical curves corresponding both to low (up to 15 $J \cdot m^{-2} \cdot s^{-½} \cdot K^{-1}$) and to high (140 $J \cdot m^{-2} \cdot s^{-½} \cdot K^{-1}$) thermal inertia values, with roughness 0.12 and 0.55, respectively, and $\chi^2 \approx 0.4$ and 1. The curves are very different from each other only outside the time interval of the retrieved temperatures. However, in the case of crater Haulani, we know that a thermal contrast with respect to Ceres's average was safely detected (see section 2), so high thermal inertia values are likely to occur. We have also analyzed two specific locations in the crater, one on the central peak and the second one on the floor, with coordinates respectively [10.58°E, 6.04°N] and [10.37°E, 5.21°N] (Figure 4). The retrieved temperature data for the first location are well fitted by a theoretical curve corresponding to a thermal inertia of 110–130 $J \cdot m^{-2} \cdot s^{-½} \cdot K^{-1}$ (with $\xi = 0.38$), compatible with the highest values already found for the whole crater. The retrieved temperatures on the floor of the crater data show higher temperature values and have a slightly different slope; these points cannot be fitted with the type of materials simulated in our code, although a slightly higher thermal inertia with respect to the one found for the peak seems to be suggested by a comparison with daily curves obtained with different values of thermal conductivity. This latter point is explained by the fact that if the thermal inertia increases then the slope of diurnal temperature curve decreases, and the floor points have a slightly smaller slope. An enhancement of thermal inertia causes the temperature to drop, the roughness being equal, but if the roughness increases then the temperature rises; we could say that the higher thermal solution for the floor is possible because the roughness may be higher with respect to the peak point.

#### 3.1.2. The Occator Crater

For the analysis of this crater we selected two areas, fully contained in the bright spots regions (Table 4). In this case the analysis has been more difficult because the areas are very small and, as a consequence, the number of data points useful for the analysis is lower (typically few dozens of points for each area). In

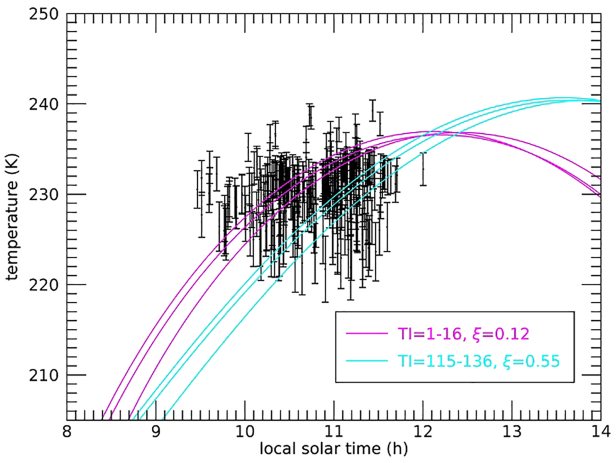


**Figure 3.** Comparison between theoretical (solid lines) and observed (black bars) temperatures for the whole selected area of the Haulani crater. Thermal inertia is expressed in $J \cdot m^{-2} \cdot s^{-½} \cdot K^{-1}$.

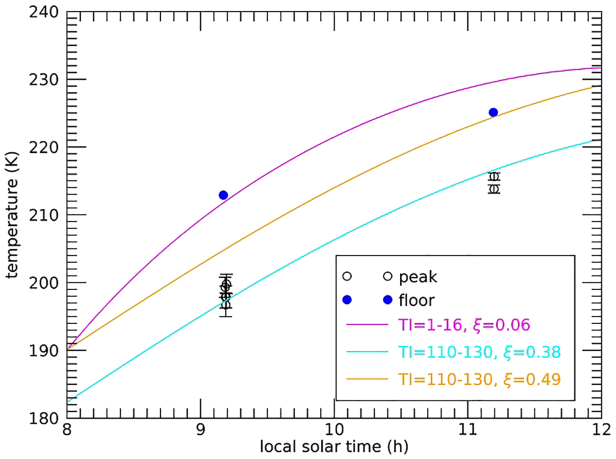


**Figure 4.** Comparison between theoretical (solid lines) and observed (black bars) temperatures for the peak in the Haulani crater. The thermal inertia derived from the model is 120 ± 10 J·m$^{-2}$·s$^{-½}$·K$^{-1}$. The blue dots refer to the floor (see text), and the magenta line refers to a thermal inertia equal to the Ceres's average. For the comparison with the average thermal inertia of Ceres a roughness $\xi = 0.06$ was assumed in order to have temperatures comparable with the floor points. The error bars of the floor points are small and are not visible at the scale of the picture.

Figures 5a and 5b we display the theoretical temperature curves compared with the retrieved temperature data: Figure 5a represents the best fit obtained for Cerealia Facula, while Figure 5b shows the best fit obtained for Vinalia Facula. The observed temperatures in the case of Vinalia Facula data are fitted by theoretical curves corresponding to fine dust (thermal inertia up to 15 J·m$^{-2}$·s$^{-½}$·K$^{-1}$ and roughness 0.55), but regolith material, with thermal inertia around 120–130 J·m$^{-2}$·s$^{-½}$·K$^{-1}$ ($\xi = 0.6 - 0.9$), are also compatible with the data.

The analysis of Cerealia Facula has given similar results, although here low thermal inertia curves provide a worse fit. Therefore, there cannot be a unique solution. To be sure, on the basis of VIR data, no thermal anomaly was revealed in these faculae down to a spatial resolution of 0.38 km per pixel; since a higher value of the thermal inertia would imply that, at a given local solar time, the surface would be cooler than a lower thermal inertia surface, we could infer that the lower thermal inertia solution is the preferred interpretation.

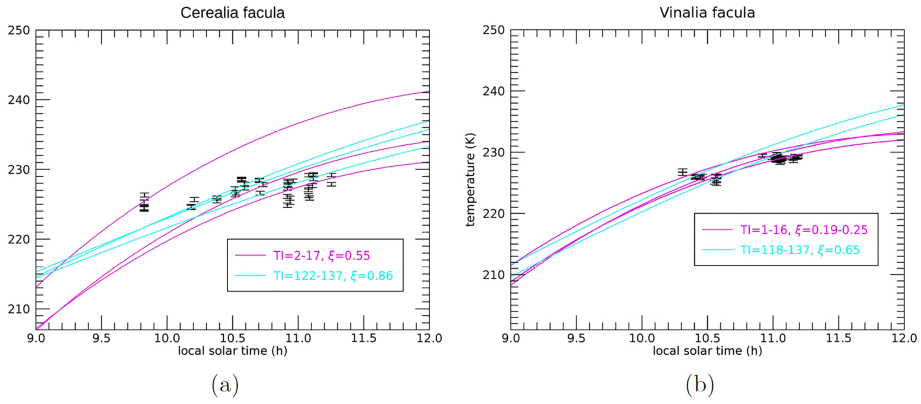


**Figure 5.** Comparison between theoretical (magenta and cyan lines) and observed (black bars) temperatures for the bright faculae found in the floor of crater Occator. Figures 5a and 5b refer to Cerealia Facula and to Vinalia Facula, respectively. The cyan curves are calculated assuming the presence of regolith, a material coarser than dust, corresponding to a thermal inertia up to about 140 J·m$^{-2}$·s$^{-½}$·K$^{-1}$, while the magenta curves are calculated assuming the fine dust (thermal inertia up to 15 J·m$^{-2}$·s$^{-½}$·K$^{-1}$).

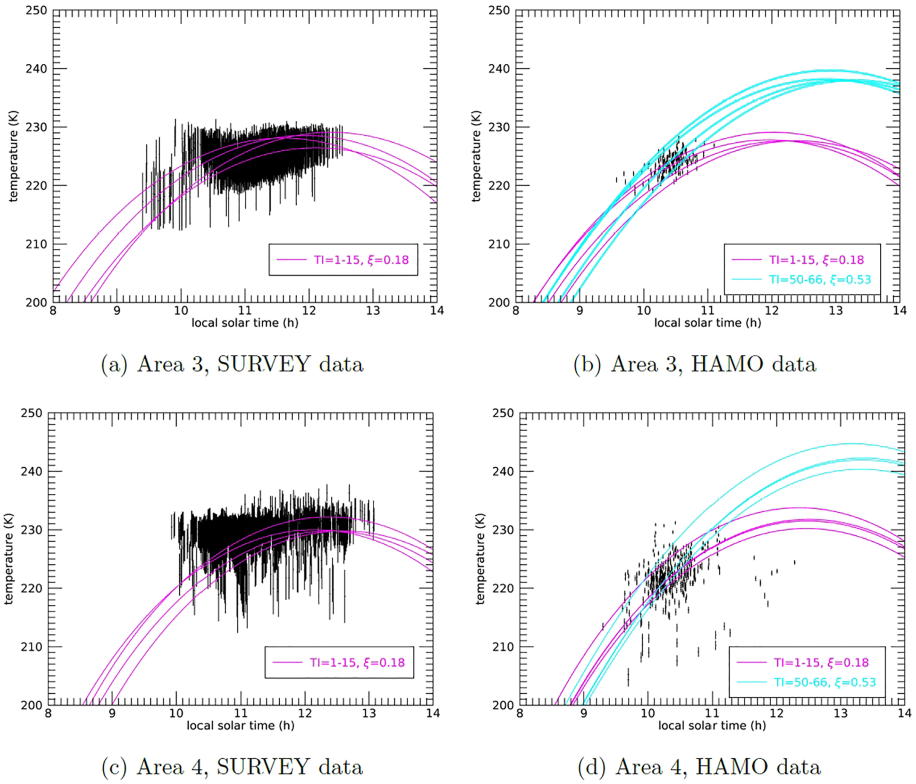


**Figure 6.** Comparison between theoretical (continuous lines) and retrieved (black dots plus black error bars) surface temperatures for Areas 3 and 4; we assume the presence on the surface of very fine dust (magenta lines) and fine regolith (cyan lines). (a) SURVEY data and a surface covered by fine dust (magenta lines); (b) HAMO data and a surface covered by fine dust (magenta lines) or fine regolith (cyan lines); (c) SURVEY data and a surface covered by fine dust (magenta lines); (d) HAMO data and a surface covered by fine dust (magenta lines) or fine regolith (cyan lines). Thermal inertia is expressed in $J \cdot m^{-2} \cdot s^{-1/2} \cdot K^{-1}$. HAMO = High Altitude Mapping Orbit.

### 3.2. Average Thermal Inertia

An analysis has been performed on the regions of Ceres that did not show textural or compositional differences with respect to the rest of the surface. The results of this analysis are summarized in Figure 6 and Table 5. The plots show the comparison between the retrieved temperature data (shown as black dots with error bars) with the theoretical temperature curves (shown as lines); they refer to Areas 3 and 4 (see Table 5), but the results for the other areas listed in Table 5 are very similar. Every theoretical temperature profile refers to a specific location, selected from the set of observed points. In our analysis we considered VIR data acquired in both the Survey and HAMO mission phases. The data acquired during these phases have been used in this work because they display a good tradeoff between coverage and pixel resolution compared to the data from the other phases of the mission. As can be noticed, the higher resolution of HAMO seems to confirm the results found with earlier Survey data; $\chi^2$ values are typically between few tenths and the unit.

## 4. Discussion

It should be noted that in most cases separating the effects of thermal inertia and subpixel roughness is challenging, because, due to the limited temporal coverage of the observed points, the data can be fitted by theoretical temperature curves calculated with different couples of ($k$, $\xi$): in principle, the same result could be obtained by fitting the data with a higher value of $k$ and a lower value of X (high $\xi$) or a lower value of $k$ and a higher value of $X$ (low $\xi$). As thermal inertia increases, the maximum daytime temperature value decreases and its position in local solar time moves from the local noon to the afternoon: The position of the peak temperature is then a diagnostic quantity that could disentangle the combined effects of the thermal conductivity and roughness (Delbo et al., 2015). Unfortunately, due to the limited coverage of the HAMO data considered

in our analysis in terms of local solar time, with a typical coverage of 2 to 3 hr in the local morning, the peak temperature and its position are never available. VIR data acquired in the earlier Survey phase cover a larger interval of local solar time values and include the local noon, but HAMO data display a pixel resolution ~2.9 times higher on average. Nighttime temperatures would also constrain thermal inertia very effectively (Delbo et al., 2015), but as we clarified earlier, VIR has no access to such low temperature values.

Another key point is our roughness model: The temperatures have been derived from DAWN radiance measurements and as such they are dependent on the observations geometry and not only on the illumination geometry. So a more realistic, and computationally heavy, directional roughness model should be applied in order to improve the analysis; this will be done in a near future.

The thermal conductivity is temperature dependent and so is thermal inertia (equation (1)). When the regolith grains are small, the radiative heat transfer is dominant because the surface contact between grains is small, and the solid-state heat conduction (transfer by phonons) is less efficient; in this case the conductivity is small and is very sensitive to the temperature because the radiative heat transfer is proportional to $T^3$. If the grain size increases then the transfer by phonons becomes dominant, the conductivity increases and is less sensitive to the temperature (see, e.g., Hale & Hapke, 2002, in which these effects are well discussed). In the simulations of the fine dust the thermal inertia is dominated by the radiative transfer, and the range of about 1–15 $J{\cdot}m^{-2}{\cdot}s^{-½}{\cdot}K^{-1}$ depicted for the average value corresponds to the temperature range of the simulation (70–240 K, that is the full diurnal temperature cycle; see section 2.2); in the case of the material defined as "regolith" (that has been used for the faculae and the Haulani crater) the grains are larger and the thermal inertia has lower relative oscillations.

The Haulani crater is expected to have a higher than the average thermal inertia because it shows a thermal contrast with respect to other areas of Ceres with equal or similar illumination conditions (Tosi et al., 2018). The average albedo of the area and of the two selected points (peak and floor, inside the crater) is about 0.04, similar to the Ceres's average, so we can safely conclude that albedo plays a marginal role in the VIR-measured daytime temperatures. The high thermal inertia is consistent instead with the higher compactness of Haulani crater as seen by the FC (Tosi et al., 2019); the peak located at the center of the crater appears to have a particularly compact surface. The overall temperature data in the crater hint at a thermal inertia up to 140 $J{\cdot}m^{-2}{\cdot}s^{-½}{\cdot}K^{-1}$; in particular, the data of the peak are well fitted by a theoretical curve with a thermal inertia of 130 $J{\cdot}m^{-2}{\cdot}s^{-½}{\cdot}K^{-1}$. The high slopes on the peak could be steeper than the angle of repose, and this could explain a less fine-grained material on steep slopes. The point in the floor has a similar situation because it shows higher temperature values at the same local solar times, so a similar thermal inertia and/or higher roughness could explain the observed data, but this point is still unclear because the FC images show that the floor material appears to be less compact than the peak. We can conclude that, while the results of the model seem to support a wide range of thermal inertia values, further considerations (the existence of a thermal contrast and the compactness of the floor material seen in the images of the FC) are a clear indication in favor of the higher thermal inertia values.

The bright spots in crater Occator have a daily temperature curve that is compatible with both low (1–17 $J{\cdot}m^{-2}{\cdot}s^{-½}{\cdot}K^{-1}$) and high thermal inertia (up to about 140 $J{\cdot}m^{-2}{\cdot}s^{-½}{\cdot}K^{-1}$). The interpretation is not straightforward. Spectral unmixing carried out by Raponi et al. (2017) suggest that the grain size of the surface regolith in the faculae could be smaller or anyway compatible with the average grain size of the surface of Ceres; this conclusion would agree with a low thermal inertia, because the thermal inertia we obtain from the fit is more sensitive to the roughness than to the albedo, and we know that if the grain size increases then thermal inertia increases. Furthermore, no thermal anomaly has been detected in these faculae. However, Longobardo et al. (2017) performed a thorough photometric analysis of the faculae, finding that the phase curve has the same steepness of the average of Ceres despite their larger albedo; they propose that this could be due to a mixing of bright and dark material (similar to what happens on Vesta) or a larger grain size and/or a larger roughness. The roughness could be explained by the young age of Occator: the surface of the faculae has not been yet leveled because not enough time is passed, so some surface irregularity is still present today. Moreover, the brines that reached the surface from the interior are not evenly distributed. The data from the so called Extended mission phase (from May 2016 to July 2018), which will be the subject a future work, could maybe give a more clear indication on the real thermal inertia range of values of this area, and strengthen our conclusions.

As for the average thermal inertia on the surface of Ceres, a low thermal inertia value (corresponding to values comprised between 1 and 15 ($J \cdot m^{-2} \cdot s^{-½} \cdot K^{-1}$), hinting to dust or very fine-grained regolith), with $\xi \approx 0.2$, is a possible solution for the areas analyzed in this work (Table 5), but a theoretical curve with thermal inertia ≈50–60 ($J \cdot m^{-2} \cdot s^{-½} \cdot K^{-1}$) and roughness $\xi \approx 0.5$, corresponding to a much coarser material, could also fit the data. The determination of thermal inertia carried out earlier for Vesta was based on coarse resolution data obtained in the Approach phase, which displayed a broad coverage in terms of local solar time. In our case, we attempted the same analysis relying mostly on HAMO data, which have a good pixel resolution but a relatively narrow coverage in terms of local solar time. In this case, a check can come from the previous analysis of the disk-integrated thermal inertia: the low thermal inertia values we have obtained compare well with previous observations and modeling. Similar values were found by Müller and Lagerros (1998), that is, 20 $J \cdot m^{-2} \cdot s^{-½} \cdot K^{-1}$; Spencer et al. (1989) and Chamberlain et al. (2009), that is, 15 $J \cdot m^{-2} \cdot s^{-½} \cdot K^{-1}$. Keihm et al. (2013) found a slightly higher value (80 $J \cdot m^{-2} \cdot s^{-½} \cdot K^{-1}$). Titus (2015) calculated Ceres's surface temperature by setting a thermal inertia range from 11 to 42 $J \cdot m^{-2} \cdot s^{-½} \cdot K^{-1}$, in order to constrain the origin of the water vapor plumes above the surface. For this reason, we feel confident that a low thermal inertia value comprised between 1 and 15 $J \cdot m^{-2} \cdot s^{-½} \cdot K^{-1}$, implying a surface covered by a layer of very fine dust, is the best solution and is representative of the average thermal inertia of the surface of the body.

Delbo and Tanga (2008) have found a decreasing trend of thermal inertia as function of diameter for the small bodies in the Main Asteroid Belt. This trend is easily explained: a large body in the Main Belt develops a soil of fine dust and/or regolith over hundreds of millions of years of evolution and exposure to the space environment. Instead, smaller bodies are often the result of a disruptive event, and their smaller gravity make it difficult to retain smaller particles. In this context our results are plausible: they imply a surface covered by a layer of very fine dust, as could be expected for a body as large as Ceres. This does not imply that the surface is necessarily uniform: areas corresponding to fresher, younger craters, or areas showing a recent deposition of materials such as brines, could well display higher thermal inertia values due to the physical characteristics of the surface. The values found for Haulani crater, similar to the values determined for objects much smaller and with a different collisional history such as (101955) Bennu (Emery et al., 2019) and (162173) Ryugu (Shimaki et al., 2019), are probably hinting at a surface on which coarse regolith prevails over dust.

## 5. Conclusions

Prior to the arrival of the National Aeronautics and Space Administration Dawn mission at Ceres, estimates of the average thermal inertia of its surface have been published by several authors, but, using for the first time disk-resolved data at good spatial resolution (0.4–1.1 km), we have independently derived thermal inertia values for the surface. We have used an approach similar to the one previously used for the large asteroid Vesta by Capria et al. (2014), but using data with better spatial resolution, obtained in both the Survey (1.1 km per pixel) and HAMO (0.38 km per pixel) mission phases. We performed a detailed study of two geologically young areas with peculiar mineralogy (Cerealia and Vinalia faculae in crater Occator, and the floor of crater Haulani).

Given its young age (<6 Ma), the floor of crater Haulani could still be compact enough and shows a remarkable thermal contrast, especially in its central mountainous ridge, so a higher thermal inertia with respect to the Ceres's average is indeed expected; we have found an average value up to 140 $J \cdot m^{-2} \cdot s^{-½} \cdot K^{-1}$ for the whole area selected in the crater, and the data of the central peak are well fitted by a curve with 110–130 $J \cdot m^{-2} \cdot s^{-½} \cdot K^{-1}$.

For crater Occator's faculae the thermal inertia could be comparable with the average value of Ceres, and this possibility has to be compared with other results coming from spectral unmixing of the same region. Other studies could indicate larger grain sizes of the surface regolith, and higher values of thermal inertia are also compatible with the data.

The results for the average thermal inertia are compatible with a generally low value of the thermal inertia: in most cases, the observed temperature curves are best fitted by theoretical thermal conductivities typical of materials as fine dust (thermal inertia between about 1 and 15 $J \cdot m^{-2} \cdot s^{-½} \cdot K^{-1}$), although higher values (up to 60 $J \cdot m^{-2} \cdot s^{-½} \cdot K^{-1}$) cannot be excluded.

**Acknowledgments**

The VIR project is funded by the Italian Space Agency (ASI), ASI-INAF Contract I/004/12/0. VIR was developed under the leadership of the Istituto di Astrofisica e Planetologia Spaziale (INAF-IAPS), Rome, Italy. The instrument was built by Selex-Galileo, Florence, Italy. Support of the Dawn Science, Instrument, Operations Teams, as well as of the Dawn at Vesta Participating Scientist program, is gratefully acknowledged. We also acknowledge the hard work carried out by Robert Gaskell in providing a detailed shape model that was used in this work to properly model the data. Dawn data are archived in NASA's Planetary Data System; VIR spectral data may be obtained at https://sbn.psi.edu/pds/resource/dawn/ website. The computational resources used in this research have been supplied by INAF-IAPS through the DataWell project.

## References

Acton, C. H. (1996). Ancillary data services of NASA's Navigation and Ancillary Information Facility. *Planetary and Space Science*, *44*(1), 65–70. https://doi.org/10.1016/0032-0633(95)00107-7

Ammannito, E., DeSanctis, M. C., Ciarniello, M., Frigeri, A., Carrozzo, F. G., Combe, J. P., et al. (2016). Distribution of phyllosilicates on the surface of Ceres. *Science*, *353*(6303), aaf4279. https://doi.org/10.1126/science.aaf4279

Audouard, J., Poulet, F., Vincendon, M., Bibring, J. P., Forget, F., Langevin, Y., & Gondet, B. (2014). Mars surface thermal inertia and heterogeneities from OMEGA/MEX. *Icarus*, *233*, 194–213. https://doi.org/10.1016/j.icarus.2014.01.045

Biele, J., Pelivan, I., Kuhrt, E., Davidsson, B., Choukroun, M., & Alexander, C. J. (2014). Recommended values and correlations of thermophysical properties for comet modelling, American Geophysical Union, Fall Meeting 2014, abstract id. P41C-3915

Capria, M. T., Tosi, F., de Sanctis, M. C., Capaccioni, F., Ammannito, E., Frigeri, A., et al. (2014). Vesta surface thermal properties map. *Geophysical Research Letters*, *41*, 1438–1443. https://doi.org/10.1002/2013GL059026

Carrozzo, F. G., de Sanctis, M. C., Raponi, A., Ammannito, E., Castillo-Rogez, J., Ehlmann, B. L., et al. (2018). Nature, formation, and distribution of carbonates on Ceres. *Science Advances*, *4*(3), e1701645. https://doi.org/10.1126/sciadv.1701645

Chamberlain, M. A., Lovell, A. J., & Sykes, M. V. (2009). Submillimeter photometry and lightcurves of Ceres and other large asteroids. *Icarus*, *202*(2), 487–501. https://doi.org/10.1016/j.icarus.2009.03.002

Ciarniello, M., de Sanctis, M. C., Ammannito, E., Raponi, A., Longobardo, A., Palomba, E., et al. (2017). Spectrophotometric properties of dwarf planet Ceres from the VIR spectrometer on board the Dawn mission. *Astronomy & Astrophysics*, *598*, A130. https://doi.org/10.1051/0004-6361/201629490

Combes, J. P., McCord, T. B., Tosi, F., Ammannito, E., Carrozzo, F. G., De Sanctis, M. C., et al. (2016). Detection of local $H_2O$ exposed at the surface of Ceres. *Science*, *353*(6303).

Cremers, C. J., & Hsia, H. S. (1973). Thermal conductivity and diffusivity of Apollo 15 fines at low density, *Proceedings of the Fourth Lunar Science Conference* (Supplement 4, Geochimica and Cosmochimica Acta), **3**.

Davidsson, B. J. R., Rickman, H., Bandfield, J. L., Groussin, O., Gutierrez, P. J., Wilska, M., et al. (2015). Interpretation of thermal emission. I. The effect of roughness for spatially resolved atmosphereless bodies. *Icarus*, *252*, 1–21. https://doi.org/10.1016/j.icarus.2014.12.029

De Meo, F. E., Alexander, C. M., Walsh, K. J., Chapman, C. R., & Binzel, R. P. (2015). The compositional structure of the asteroid belt. In P. Michel, et al. (Eds.), *Asteroids IV*, (pp. 107–128). Tucson: Univ. of Arizona. DOI: 10.2458/azu_uapress_9780816532131-ch006

De Sanctis, M. C., Ammannito, E., Carrozzo, F. G., Ciarniello, M., Giardino, M., Frigeri, A., et al. (2018). Ceres's global and localized mineralogical composition determined by Dawn's Visible and Infrared Spectrometer (VIR). *Meteoritics & Planetary Science*, *53*, 1884–1901.

De Sanctis, M. C., Coradini, A., Ammannito, E., Filacchione, G., Capria, M. T., Fonte, S., et al. (2011). The VIR spectrometer. *Space Science Reviews*, *163*(1-4), 329–369. https://doi.org/10.1007/s11214-010-9668-5

De Sanctis, M. C., Raponi, A., Ammannito, E., Ciarniello, M., Toplis, M. J., McSween, H. Y., et al. (2016). Bright carbonate deposits as evidence of aqueous alteration on (1) Ceres. *Nature*, *536*(7614), 54–57. https://doi.org/10.1038/nature18290

Delbo, M., Mueller, M., Emery, J. P., Rozitis, B., & Capria, M. T. (2015). Asteroid thermophysical modeling. In P. Michel, et al. (Eds.), *Asteroids IV*, (pp. 107–128). Tucson: Univ. of Arizona. DOI: 10.2458/azu_uapress_9780816532131-ch006

Delbo, M., & Tanga, P. (2008). Thermal inertia of main belt asteroids smaller than 100 km from IRAS data. *Planetary and Space Science*, *257*, 259–265.

Emery, J. P., Rozitis, B., Christensen, P. R., Hamilton, V. E., Simon, A. A., Reuter, D. C., et al. (2019). Thermophysical properties of (101955) Bennu from OSIRIS-REx observations, LPSC 2019, no. 2582

Hale, A. S., & Hapke, B. (2002). A time-dependent model of radiative and conductive thermal energy transport in planetary regoliths with applications to the Moon and Mercury. *Icarus*, *156*(2), 318–334. https://doi.org/10.1006/icar.2001.6768

Harris, A. W., & Lagerros, J. S. V. (2002). Asteroids in the thermal infrared. In W. F. Bottke, et al. (Eds.), *Asteroids III*, (pp. 205–218). Tucson, Ariz: Univ. of Arizona Press.

Jaumann, R., Preusker, F., Krohn, K., von der Gathen, I., Stephan, K., Matz, K. D., et al. (2017). Topography and geomorphology of the interior of Occator crater on Ceres, EPSC Abstract, 11

Keihm, S., Kamp, L., Gulkis, S., Hofstadter, M., Lee, S., Janssen, M., & Choukroun, M. (2013). Reconciling main belt asteroid spectral flux density measurements with a self-consistent thermophysical model. *Icarus*, *226*(1), 1086–1102. https://doi.org/10.1016/j.icarus.2013.07.005

Keihm, S., Tosi, F., Kamp, L., Capaccioni, F., Gulkis, S., Grassi, D., et al. (2012). Interpretation of combined infrared, submillimeter, and millimeter thermal flux data obtained during the Rosetta fly-by of Asteroid (21) Lutetia. *Icarus*, *221*(1), 395–404. https://doi.org/10.1016/j.icarus.2012.08.002

Lagerros, J. S. V. (1998). Thermal physics of asteroids IV. Thermal infrared beaming. *Astronomy and Astrophysics*, *332*, 1123–1132.

Longobardo, A., Palomba, E., Carrozzo, F. G., Galiano, A., de Sanctis, M. C., Stephan, K., et al. (2019). Mineralogy of the Occator Quadrangle. *Icarus*, *318*, 205–211. https://doi.org/10.1016/j.icarus.2017.09.022

Longobardo, A., Palomba, E., Galiano, A., de Sanctis, M. C., Ciarniello, M., Raponi, A., et al. (2017). Photometry of Ceres and Occator faculae as inferred from VIR/Dawn data. *Icarus*, *320*, 97–109. https://doi.org/10.1016/j.icarus.2018.02.022

McCord, T. B., & Sotin, C. (2005). Ceres: Evolution and current state. *Journal of Geophysical Research*, *110*, E05009. https://doi.org/10.1029/2004JE002244

Müller, T. G., & Lagerros, J. S. V. (1998). Asteroids as far-infrared photometric standards for ISOPHOT. *Astronomy and Astrophysics*, *338*, 340–352.

Nathues, A., Hoffmann, M., Platz, T., Thangjam, G. S., Cloutis, E. A., Reddy, V., et al. (2016). FC colour images of dwarf planet Ceres reveal a complicated geological history. *Planetary and Space Science*, *134*, 122–127. https://doi.org/10.1016/j.pss.2016.10.017

Nathues, A., Hoffmann, M., Schaefer, M., le Corre, L., Reddy, V., Platz, T., et al. (2015). Sublimation in bright spots on (1) Ceres. *Nature*, *528*(7581), 237–240. https://doi.org/10.1038/nature15754

Neugebauer, G., Miinch, G., Kieffer, H., Chase, S. C.,. J., & Miner, E. (1971). Mariner 1969 infrared radiometer results: Temperatures and thermal properties of the Martian surface. *Astronomical Journal*, *76*, 719. https://doi.org/10.1086/111189

Opeil, C. P., Consolmagno, G. J., Safarik, D. J., & Britt, D. T. (2012). Stony meteorite thermal properties and their relationship with meteorite chemical and physical states. *Meteoritics & Planetary Science*, *47*(3), 319–329. https://doi.org/10.1111/j.1945-5100.2012.01331.x

Palomba, E., Longobardo, A., de Sanctis, M. C., Stein, N. T., Ehlmann, B., Galiano, A., et al. (2019). Compositional differences among Bright Spots on the Ceres surface. *Icarus*, *320*(202-212), 202–212. https://doi.org/10.1016/j.icarus.2017.09.020

Park, R. S., Konopliv, A. S., Bills, B. G., Rambaux, N., Castillo-Rogez, J. C., Raymond, C. A., et al. (2016). A partially differentiated interior for (1) Ceres deduced from its gravity field and shape. *Nature*, *537*(7621), 515–517. https://doi.org/10.1038/nature18955

Platz, T., Nathues, A., Schorghofer, N., Preusker, F., Mazarico, E., Schröder, S. E., et al. (2016). Surface water-ice deposits in the northern shadowed regions of Ceres. *Nature Astronomy*, *1*, 7.

Prettyman, T. H., Feldman, W. C., McSween, H. Y., Dingler, R. D., Enemark, D. C., Patrick, D. E., et al. (2011). Dawn's gamma ray and neutron detector. *Space Science Reviews*, *163*(1-4), 371–459. https://doi.org/10.1007/s11214-011-9862-0

Preusker, F., Scholten, F., Matz, K.-D., Elgner, S., Jaumann, R., Roatsch, T., et al. (2016). Dawn at Ceres–Shape Model and Rotational State. 47th Lunar and Planetary Science Conference, no. *1903*

Raponi, A., Carrozzo, F. G., Zambon, F., de Sanctis, M. C., Ciarniello, M., Frigeri, A., et al. (2017). Mineralogical mapping of Coniraya quadrangle of the dwarf planet Ceres. *Icarus*, *318*, 99–110. https://doi.org/10.1016/j.icarus.2017.10.023

Raymond, C. A., Jaumann, R., Nathues, A., Sierks, H., Roatsch, T., Preusker, F., et al. (2011). The Dawn topography investigation. *Space Science Reviews*, *163*(1-4), 487–510. https://doi.org/10.1007/s11214-011-9863-z

Rivkin, A. S., Li, J. Y., Milliken, R. E., Lim, L. F., Lovell, A. J., Schmidt, B. E., et al. (2011). The surface composition of Ceres. *Space Science Reviews*, *163*(1-4), 95–116. https://doi.org/10.1007/s11214-010-9677-4

Roatsch, T., Kersten, E., Matz, K.-D., Preusker, F., Scholten, F., Jaumann, R., et al. (2016). High-resolution Ceres high altitude mapping orbit atlas derived from Dawn Framing Camera images. *Planetary and Space Science*, *129*, 103–107. https://doi.org/10.1016/j.pss.2016.05.011

Rozitis, B., & Green, S. F. (2011). Directional characteristics of thermal-infrared beaming from atmosphereless planetary surfaces—A new thermophysical model. *Monthly Notices of the Royal Astronomical Society*, *415*(3), 2042–2062. https://doi.org/10.1111/j.1365-2966.2011.18718.x

Russell, C. T., Raymond, C. A., Ammannito, E., Buczkowski, D. L., de Sanctis, M. C., Hiesinger, H., et al. (2016). Dawn arrives at Ceres: Exploration of a small, volatile-rich world. *Science*, *353*(6303), 1008–1010. https://doi.org/10.1126/science.aaf4219

Shimaki, Y., Senshu, H., Sakatani, N., Fukuhara, T., Tanaka, S., Arai, T., et al. (2019). Surface roughness and thermal inertia of asteroid Ryugu inferred from TIR on Hayabusa 2, LPSC 2019, no. 1724

Sierks, H., Keller, H. U., Jaumann, R., Michalik, H., Behnke, T., Bubenhagen, F., et al. (2011). The Dawn framing camera. *Space Science Reviews*, *163*(1-4), 263–327. https://doi.org/10.1007/s11214-011-9745-4

Spencer, J. R., Lebofsky, L. A., & Sykes, M. V. (1989). Systematic biases in radiometric diameter determinations. *Icarus*, *78*(2), 337–354. https://doi.org/10.1016/0019-1035(89)90182-6

Stein, N. T., Ehlmann, B. L., Palomba, E., de Sanctis, M. C., Nathues, A., Hiesinger, H., et al. (2017). The formation and evolution of bright spots on Ceres. *Icarus*, in press, *320*, 188–201. https://doi.org/10.1016/j.icarus.2017.10.014

Titus, T. N. (2015). Ceres: Predictions for near-surface water ice stability and implications for plume generating processes. *Geophysical Research Letters*, *42*, 2130–2136. https://doi.org/10.1002/2015GL063240

Tosi, F., Capria, M. T., de Sanctis, M. C., Combe, J. P., Zambon, F., Nathues, A., et al. (2014). Thermal measurements of dark and bright surface features on Vesta as derived from Dawn/VIR. *Icarus*, *240*, 36–57. https://doi.org/10.1016/j.icarus.2014.03.017

Tosi, F., Carrozzo, F. G., Raponi, A., de Sanctis, M. C., Thangjam, G., Zambon, F., et al. (2018). Mineralogy and temperature of crater Haulani on Ceres. *Meteoritics & Planetary Science*, *53*(9), 1902–1924. https://doi.org/10.1111/maps.13078

Tosi, F., Carrozzo, F. G., Zambon, F., Ciarniello, M., Frigeri, A., Combe, J. P., et al. (2019). Mineralogical analysis of the Ac-H-6 Haulani quadrangle of the dwarf planet Ceres. *Icarus*, *318*, 170–187. https://doi.org/10.1016/j.icarus.2017.08.012

Vasavada, A. R., Bandfield, J. L., Greenhagen, B. T., Hayne, P. O., Siegler, M. A., Williams, J. P., & Paige, D. A. (2012). Lunar equatorial surface temperatures and regolith properties from the Diviner Lunar Radiometer Experiment. *Journal of Geophysical Research*, *117*, E00H18. https://doi.org/10.1029/2011JE003987

Vasavada, A. R., & Paige, D. A. (1999). Near-surface temperatures on Mercury and the Moon and the stability of polar ice deposits. *Icarus*, *141*, 173–193.